Chinese Physics B

Reversible self-intercalation in trilayer 1T-$NiTe_2$

To cite this article before publication: Qian Fang *et al* 2026 *Chinese Phys. B* in press https://doi.org/10.1088/1674-1056/ae64d7

Reversible self-intercalation in trilayer 1T-$NiTe_2$

Qian Fang (方迁)[1,2], Zihao Huang (黄子豪)[1,2], Runnong Zhou (周润农)[1,2], Lei Tao (陶蕾)[2], Chen Liu (刘晨)[3], Xianghe Han (韩相和)[1,2], Li Huang (黄立)[1,2], Xiao Lin (林晓)[2], Hui Guo (郭辉)[1,2]*, Hui Chen (陈辉)[1,2]*, and Hong-Jun Gao (高鸿钧)[1,2]

[1] Beijing National Center for Condensed Matter Physics and Institute of Physics, Chinese Academy of Sciences, Beijing 100190, China

[2] School of Physical Sciences, University of Chinese Academy of Sciences, Beijing 100190, China

[3] Institute of High Energy Physics, Chinese Academy of Sciences, Beijing 100049, China

*Correspondence to: hchenn04@iphy.ac.cn, guohui@iphy.ac.cn

Self-intercalation in layered transition metal dichalcogenides provides a promising route for modulating lattice structures and electronic properties without introducing extrinsic species. As an emerging type-II Dirac semimetal, 1T-$NiTe_2$ has attracted considerable interest in the two-dimensional limit. However, reversible self-intercalation in atomically thin $NiTe_2$ has not been reported. Here, we report a reversible self-intercalation process in trilayer 1T-$NiTe_2$ synthesized on graphene substrate via van-der-Waals epitaxy. Upon post-annealing, Te desorption drives the spontaneous incorporation of Ni atoms into the van-der-Waals gaps, forming an ordered $\sqrt{3}\times\sqrt{3}$ superstructure, which can be fully reversed under Te-rich conditions. Scanning tunneling microscopy reveals the formation of this superstructure, accompanied by a modulation of the electronic states near the Fermi level. Furthermore, field emission resonance measurements demonstrate a clear modulation of the local work function induced by self-intercalation, indicative of an intercalation-driven redistribution of electronic density. Our work establishes reversible self-intercalation as an effective route for engineering superlattice potentials and tuning surface electronic properties in two-dimensional materials.

Keywords

$NiTe_2$, Self-intercalation, Van-der-Waals, Scanning tunneling microscopy

PACS

71.20.Tx, 07.79.Cz, 63.22.Np, 68.65.Cd

Introduction

Two-dimensional (2D) van-der-Waals (vdW) materials provide an exceptional platform for engineering emergent quantum states owing to their atomic thickness, weak interlayer coupling, and structural flexibility[1–7]. Among various strategies for tailoring their properties, self-intercalation, where constituent atoms occupy the vdW gaps to form additional atomic layers, has recently emerged as a powerful route for stabilizing new structural phases, including covalently bonded layered configurations, and for tuning electronic correlations beyond those accessible in pristine compounds[8–17]. This approach has enabled a variety of intriguing phenomena, such as tunable ferromagnetism in covalently bonded TaS_2[8], the emergence of Kondo physics in self-intercalated V-based layered materials[18,19], novel magnetic phases in $CrTe_2$[20–23], and modified superconductivity in $NbSe_2$[24-27]. Therefore, the unique capability of self-intercalation to couple lattice reconstruction with electronic correlations opens new opportunities for designing emergent quantum phases in low-dimensional systems.

Recently, $NiTe_2$ has attracted significant attention as a layered transition-metal dichalcogenide hosting rich electronic and topological properties. It has been identified as a type-II Dirac semimetal[28–30] and exhibits a variety of intriguing phenomena, including superconductivity[31–33], topological surface states[34,35], and thickness-dependent electronic tunability[36]. In the two-dimensional limit, additional emergent behaviors such as short-range charge density modulations[37] have also been reported, highlighting its sensitivity to structural perturbations. Beyond fundamental physics, $NiTe_2$ further demonstrates promising functionalities in catalysis[38,39] and electronic devices[40,41] such as transistor[42] and high-frequency rectifier[43], motivating extensive efforts in material synthesis for bulk crystals and ultrathin layers. Despite these advances, the exploration of self-intercalation in $NiTe_2$ remains limited. While excess Ni atoms have been reported to occupy interstitial sites and form multiple ordered phases in such a system[44], achieving uniform and well-controlled self-intercalation in atomically thin $NiTe_2$ is still challenging.

Here, we report a reversible self-intercalation process in trilayer 1T-$NiTe_2$ grown on graphene via vdW epitaxy, combining *in-situ* low-energy electron diffraction (LEED), Auger electron spectroscopy (AES), and X-ray photoelectron spectroscopy (XPS). Upon post-annealing, Te desorption drives the spontaneous intercalation of Ni atoms into the vdW gaps, leading to the formation of an ordered $\sqrt{3}\times\sqrt{3}$

superstructure. This intercalated phase can be fully reversed by annealing in a Te-rich atmosphere, restoring the pristine layered structure and enabling dynamic control of the intercalation process. Using scanning tunneling microscopy/spectroscopy (STM/STS), we directly resolve the atomic and electronic structure of the intercalated phase. Furthermore, by combining density functional theory (DFT) calculations, we reveal a modulation of the local density of states near the Fermi level, including a shift in the work function, indicating reconstruction of the electronic structure induced by the self-intercalation. Our results demonstrate reversible self-intercalation as a viable route for engineering ordered superlattice potentials and tuning electronic properties in two-dimensional quantum materials.

Results and discussion

We start with the epitaxial growth of trilayer 1T-$NiTe_2$ on bilayer graphene/SiC(0001) substrates using molecular beam epitaxy (see Methods). The 1T-$NiTe_2$ crystallizes in a vdW layered structure and hosts a hexagonal lattice with in-plane lattice constants of ~0.38 nm, as illustrated in the top and side views in Fig. 1(a). Upon post-annealing at elevated temperature under vacuum, partial desorption of Te atoms induces the formation of a self-intercalated phase [Fig. 1(b)]. The intercalation is driven by a Te-desorption-induced Ni-rich chemical potential. In this process, the excess Ni atoms in the intercalated phase is primarily generated from the $NiTe_2$ lattice interior during post-annealing, accompanied by a change in the stoichiometry of $NiTe_2$ itself. The excess Ni atoms occupy the octahedral sites within the vdW gaps, forming an additional atomic layer with a $\sqrt{3}\times\sqrt{3}$ superstructure with respect to the $NiTe_2$ lattice, thereby transforming the vdW layered structure into a covalently bonded configuration. Notably, this self-intercalated phase can be fully reversed by annealing in a Te-rich atmosphere, restoring the pristine vdW structure [Fig. 1(c)]. To track this evolution, we perform *in-situ* LEED measurements at each stage. As shown in Fig. 1(d), the as-grown trilayer $NiTe_2$ exhibits two sets of sharp diffraction spots arising from $NiTe_2$ and graphene, respectively, with nearly identical orientations, confirming epitaxial alignment. After post-annealing, an additional set of diffraction spots emerges, corresponding to a $(\sqrt{3}\times\sqrt{3})R30°$ superstructure with respect to the $NiTe_2$ lattice [Fig. 1(e)], indicative of successful self-intercalation. Following subsequent annealing in a Te-rich atmosphere, these superstructure spots disappear, leaving only the diffraction from $NiTe_2$ and graphene [Fig. 1(f)], thereby confirming the reversible de-intercalation process.

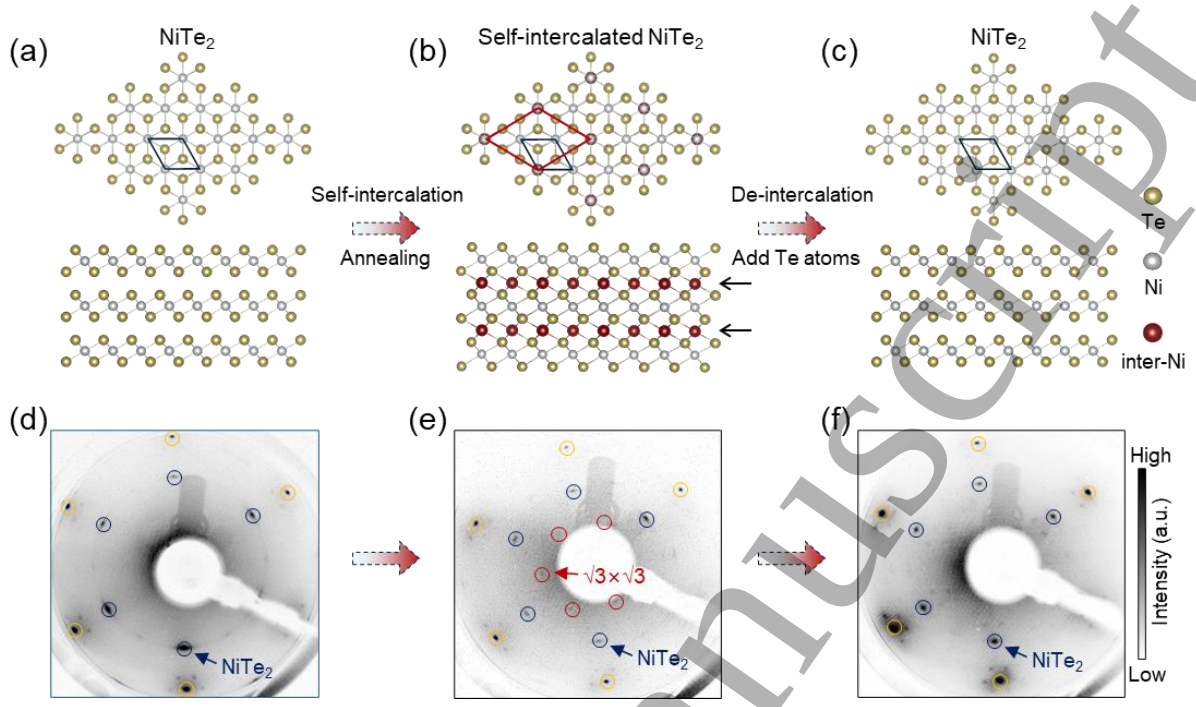

Fig. 1. Reversible self-intercalation in trilayer $NiTe_2$. (a)-(c) Schematic illustrations of the self-intercalation and de-intercalation processes of trilayer $NiTe_2$. Upon post-annealing, Ni atoms spontaneously intercalate at the vdW gaps and form a $\sqrt{3}\times\sqrt{3}$ superstructure (b). Subsequent annealing in a Te atmosphere restores the pristine $NiTe_2$ phase via de-intercalation (c). The black and red rhombuses denote the unit cells of $NiTe_2$ and the intercalation-induced superlattice, respectively. (d)-(f) Corresponding LEED patterns of the sample at stages shown in (a)-(c). The as-grown trilayer $NiTe_2$ on graphene substrate shows diffraction spots from both $NiTe_2$ (blue circles) and graphene (green circles) (d). After post-annealing, additional diffraction spots emerge (red circles), consistent with the formation of a $\sqrt{3}\times\sqrt{3}$ superlattice due to the Ni intercalation (e). These superlattice spots disappear after annealing in a Te atmosphere, showing the reversibility of the intercalation process (f).

We further study the reversible self-intercalation process using *in-situ* AES and XPS measurements. As shown in Fig. 2(a), both the pristine and post-annealed $NiTe_2$ exhibit characteristic AES signals from Ni and Te elements. Notably, after post-annealing, the intensity of the Te Auger peaks is significantly suppressed, whereas that of Ni remains nearly unchanged, indicating substantial Te desorption during the annealing process. In addition, the Ni Auger peak exhibits a slight shift toward higher kinetic energy [Fig. 2(b)], suggesting a modification of the local chemical environment of Ni atoms. Consistent with the AES results, high-resolution XPS measurements reveal pronounced changes in both composition and local chemical environment. As shown in Fig. 2(c) and 2(d), the Te 3*d* core-level intensity is markedly reduced after annealing, while the Ni 2*p* intensity remains largely unchanged, further confirming Te depletion. Meanwhile, both the Ni 2*p* and Te 3*d* core levels shift toward lower binding energy, ~1.1 eV

and ~0.5 eV, respectively. The simultaneous shift of both Ni *2p* and Te *3d* core levels toward lower binding energies indicates a substantial reconstruction of the electronic structure. This behavior cannot be explained by a simple rigid Fermi level shift, but instead reflects a combination of modified local bonding and enhanced electronic screening in the intercalated phase. These combined observations demonstrate that Te desorption drives the formation of a Ni-rich, self-intercalated phase.

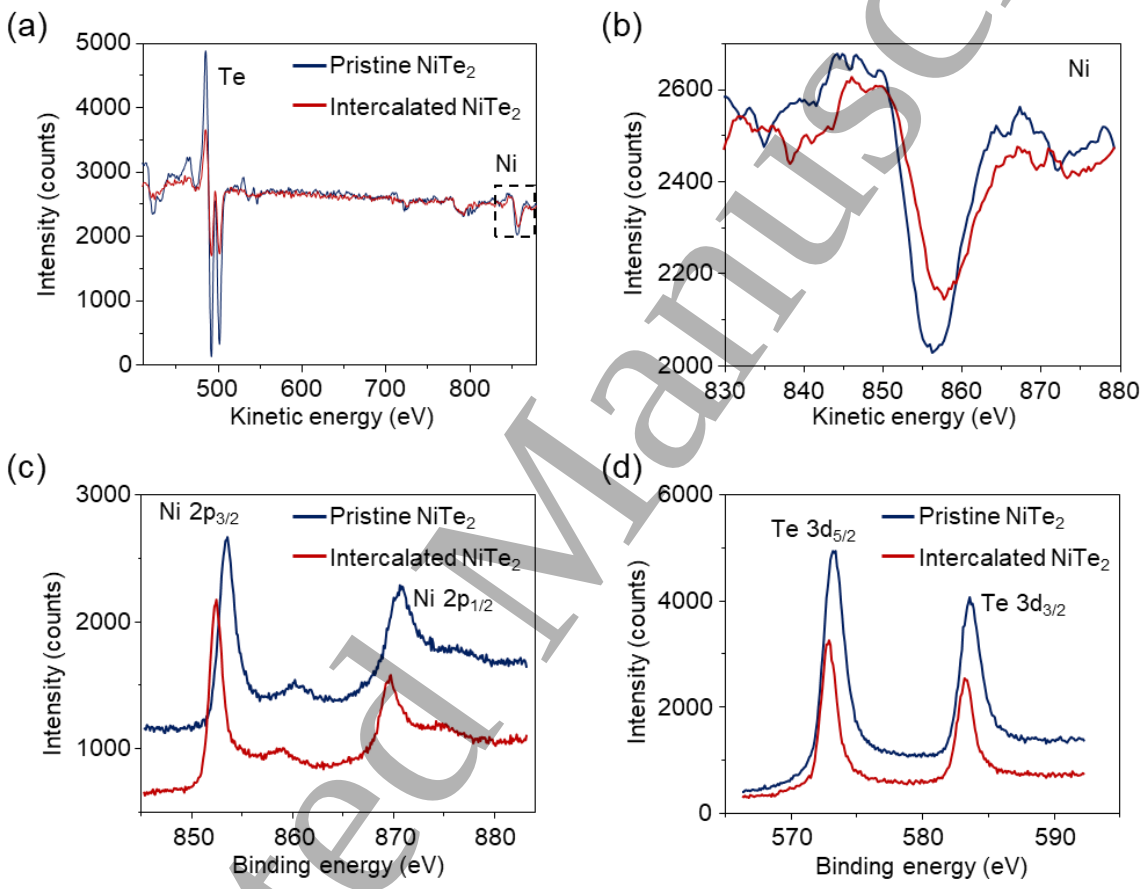

Fig. 2. AES and XPS measurements for the pristine and self-intercalated trilayer $NiTe_2$. (a) *In-situ* AES spectra of the pristine (blue) and self-intercalated $NiTe_2$ (red), both showing characteristic signals from the Te and Ni elements. (b) Zoom-in AES spectra of the Ni Auger region (black dashed rectangle), showing a slight shift of the Auger peak toward higher kinetic energy after self-intercalation. (c) XPS spectra of the Ni 2*p* core levels for pristine (blue) and self-intercalated $NiTe_2$ (red), showing a clear red shift toward lower binding energy after intercalation. (d) XPS spectra of the Te 3*d* core levels for pristine (blue) and self-intercalated $NiTe_2$ (red), also showing a noticeable shift toward lower binding energy after the self-intercalation process.

In order to study the atomic and electronic structure of the self-intercalated $NiTe_2$ phase, we carried out STM measurements. Large-scale STM topography of the as-grown sample reveals the formation of

regularly shaped $NiTe_2$ islands on the graphene surface [Fig. 3(a)]. The measured height is about 2.0 nm, consistent with a trilayer thickness [Fig. 3(b)]. Atomic-resolution STM image clearly shows a hexagonal lattice with a periodicity of ~0.38 nm, corresponding to the arrangement of the topmost Te atoms in $NiTe_2$ [Fig. 3(c)]. After post-annealing, the large-sized $NiTe_2$ islands retain their lateral morphology, while the apparent height decreases slightly to ~1.8 nm, indicating structural modification upon self-intercalation [Fig. 3(d) and 3(e)]. Notably, atomic-resolution STM image reveals an additional superstructure rotated by 30° with respect to the $NiTe_2$ lattice [Fig. 3(f)]. The measured lattice periodicity of the superstructure is ~0.66 nm, corresponding to $\sqrt{3}$ times that of the $NiTe_2$ lattice. Combined with the corresponding fast Fourier transform (FFT) patterns [Fig. 3(g) and 3(h)], these results confirm the formation of a $(\sqrt{3}\times\sqrt{3})R30°$ superstructure, in good agreement with the LEED results. Furthermore, spatially averaged dI/dV spectra acquired on pristine and self-intercalated $NiTe_2$ agree well with the DFT calculated density of states based on the corresponding structural models, further supporting the $\sqrt{3}\times\sqrt{3}$ intercalated structure [Fig. 3(i)]. Both exhibit metallic behavior, while showing a pronounced modulation of the electronic states near the Fermi level, indicative of a reconstruction of the local electronic structure induced by self-intercalation. The $\sqrt{3}\times\sqrt{3}$ superstructure is consistently observed across multiple islands with no other structural phases detected, indicating a high degree of spatial homogeneity. We also investigated the recovered $NiTe_2$ after de-intercalation under a Te-rich annealing condition. Consistent with the LEED results, STM and STS measurements show that both the lattice constant and the spectroscopic features return to those of the pristine phase, indicating recovery of the original hexagonal lattice and electronic characteristics.

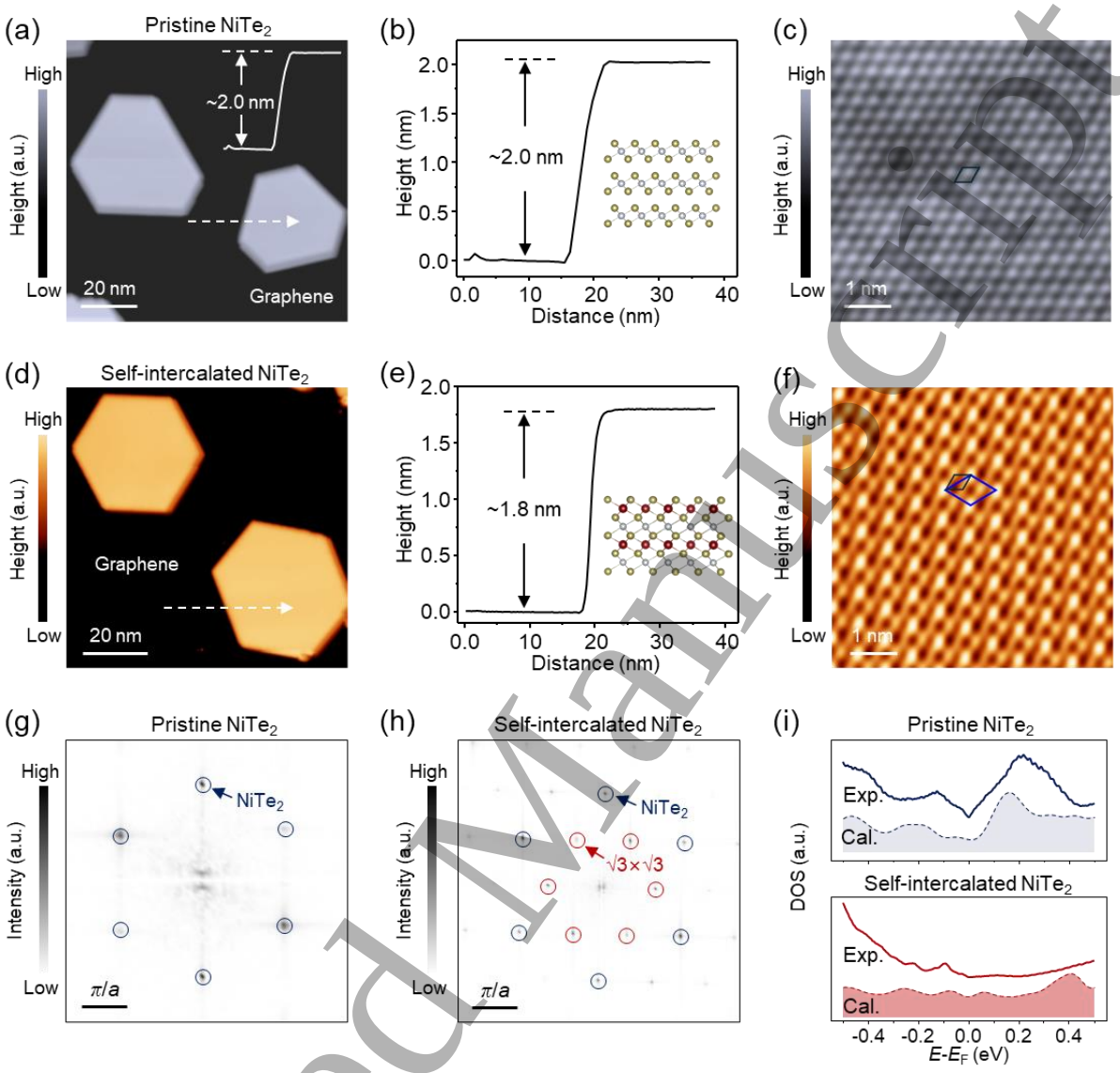

Fig. 3. Atomic and electronic structures of pristine and self-intercalated trilayer $NiTe_2$. (a) Large-scale STM topography of the trilayer $NiTe_2$ grown on graphene substrate (V_s = -1 V, I_t = 20 pA), showing regular hexagonal shape. (b) Line profile along the white dashed arrow in (a), showing a thickness of ~2.0 nm, consistent with trilayer $NiTe_2$. (c) Atomic-resolution STM image of the pristine $NiTe_2$ (V_s = -10 mV, I_t = 5 nA), showing a hexagonal lattice (black rhombus) with periodicity of ~0.38 nm. (d) Large-scale STM topography of the trilayer $NiTe_2$ after self-intercalation (V_s = -2 V, I_t = 20 pA). (e) Line profile along the white dashed arrow in (d), showing a reduced thickness of ~1.8 nm, consistent with the self-intercalated structure. (f) Corresponding atomic-resolution STM image (V_s = -0.5 V, I_t = 1 nA), showing coexistence of the hexagonal lattice of $NiTe_2$ (black rhombus) and an overlaid $\sqrt{3}\times\sqrt{3}$ superstructure (blue rhombus) with periodicity of ~0.66 nm. (g,h) Corresponding FFT patterns of (c) and (f), showing emergence of $(\sqrt{3}\times\sqrt{3})R30°$ superstructure after intercalation. (i) The typical dI/dV spectra of pristine (blue solid curve) and $\sqrt{3}\times\sqrt{3}$ self-intercalated trilayer $NiTe_2$ (red solid curve), showing both metallic nature with a pronounced difference in electronic states near the Fermi level. The blue and red covered regions are the DFT calculated density of states based on pristine and self-intercalated structure models, agreeing well with the experimental results.

Finally, the modification of the electronic states induced by self-intercalation suggests a corresponding variation in the local tunneling barrier. Since the tunneling barrier is directly related to the local work function, we probe it using field emission resonances (FER) in the STM junction, which provide a sensitive measure of the surface potential with high spatial resolution[45,46]. FER spectra, also known as Gundlach oscillations[47], arise in the Fowler–Nordheim tunneling regime[48] when the applied bias exceeds the sample work function. Under this condition, the bias-induced potential drop in the tunneling junction forms a quasi-trapezoidal barrier, supporting a series of image-potential states confined in the vacuum gap[49]. The energies of these resonances depend sensitively on the local work function, enabling spatial mapping of surface potential variations[50].

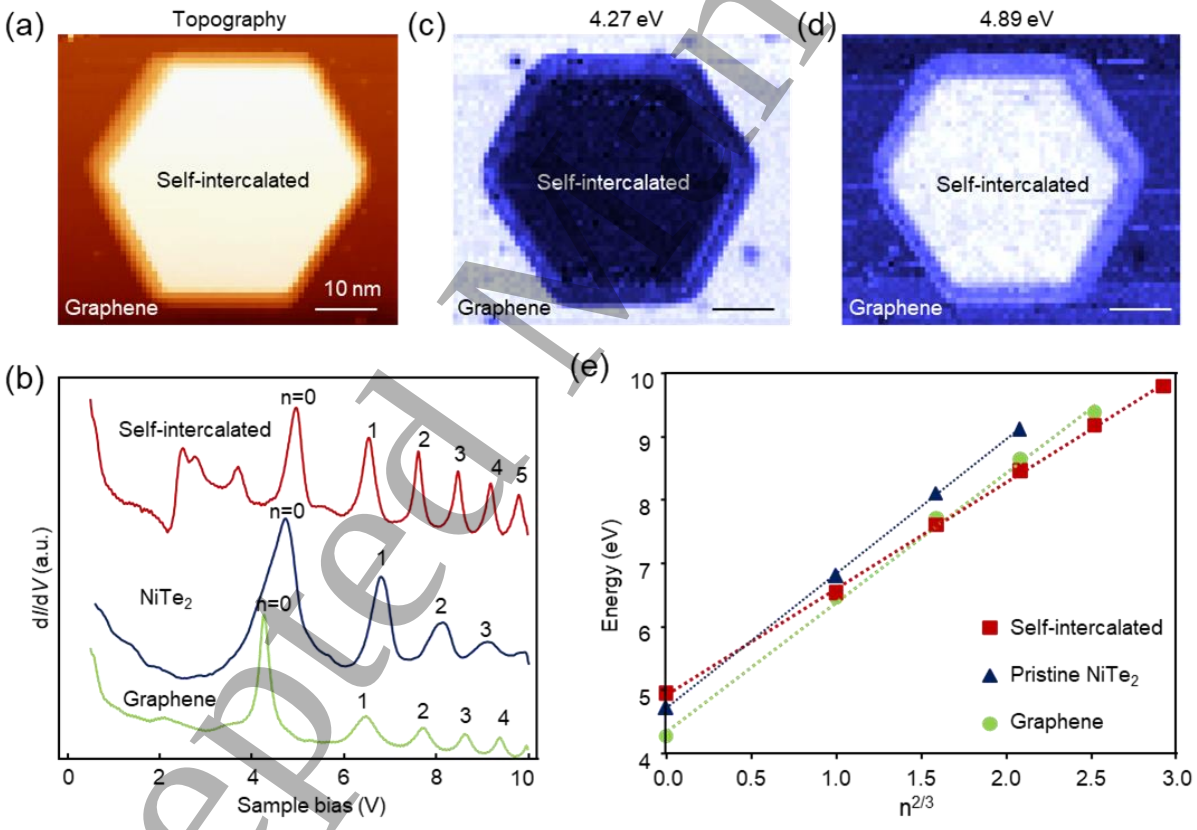

Fig. 4. Spectroscopic characterization of self-intercalated $NiTe_2$ on graphene substrate. (a) STM image of a self-intercalated $NiTe_2$ island. (b) FER spectra taken on pristine $NiTe_2$, self-intercalated $NiTe_2$ and the graphene substrate, respectively, showing a series of resonance peaks. (c, d) The dI/dV maps of FER spectra at the energy of 4.27 eV (c) and 4.89 eV (d), respectively, showing the contrast between self-intercalated $NiTe_2$ island and graphene substrate. (e) Extracted and fitted image-potential state peak positions from (b), showing the different work function of pristine $NiTe_2$, self-intercalated $NiTe_2$ and the graphene substrate. Tunneling parameters: V_s = 50 mV, I_t = 0.3 nA, V_{mod}=10 mV).

Fig. 4(a) shows the STM topography of a self-intercalated $NiTe_2$ island on the graphene substrate. FER spectra acquired on pristine $NiTe_2$, self-intercalated $NiTe_2$, and the graphene substrate exhibit a series of well-defined resonance peaks [Fig. 4(b)], corresponding to image-potential states in the vacuum tunneling gap. To a first approximation, the sample work function can be estimated from the energy of the first FER peak. From graphene to pristine $NiTe_2$ and further to self-intercalated $NiTe_2$, the spectra shift systematically toward higher energies, indicating an increase in the local work function. By extracting and fitting the image-potential states, we obtain work functions of ~4.36 eV, ~4.71 eV, and ~4.94 eV for graphene, pristine $NiTe_2$, and self-intercalated $NiTe_2$, respectively [Fig. 4(e)]. Furthermore, spatially resolved dI/dV maps at energies of 4.27 eV and 4.89 eV reveal clear contrast between the self-intercalated $NiTe_2$ island and the graphene substrate [Figs. 4(c) and 4(d)], reflecting the spatial variation of the surface potential. The increase in work function upon Ni intercalation possibly originates from a modification of the surface dipole. Intercalated Ni atoms induce a redistribution of charge, leading to partial electron depletion at the top Te layer and accumulation in the subsurface region. This results in an enhanced surface dipole pointing from the vacuum toward the sample, effectively increasing the surface potential barrier and thus the work function. These results demonstrate that self-intercalation induces a pronounced modulation of the local work function and tunneling barrier, providing direct evidence of the modified surface electronic properties.

In summary, we have demonstrated a reversible self-intercalation process in trilayer 1T-$NiTe_2$, achieved via controlled thermal annealing. Tellurium desorption drives the spontaneous incorporation of Ni atoms into the vdW gaps, leading to the formation of an ordered $\sqrt{3}\times\sqrt{3}$ superstructure, which can be fully reversed under Te-rich conditions. Combining *in-situ* diffraction, spectroscopy, and scanning probe measurements, we establish a comprehensive picture of this process, including structural transformation, chemical state evolution, and electronic modulation. In particular, self-intercalation induces a reconstruction of the local electronic states and a pronounced increase in the work function, reflecting a modification of the surface potential and tunneling barrier. These results highlight reversible self-intercalation as a controllable approach for engineering ordered superlattice potentials and tuning electronic properties in two-dimensional materials, opening new opportunities for designing emergent quantum phases and functional devices.

Methods

Sample preparation. Trilayer $NiTe_2$ films were epitaxially grown on bilayer graphene/SiC substrates via molecular beam epitaxy (MBE) under ultra-high vacuum (UHV) conditions, with a base pressure of ~5×10^{-10} mbar. The bilayer graphene was prepared by annealing a 6H-SiC(0001) substrate from 650 ℃ to 1300 ℃ over 65 s, with this process repeated 80 times. $NiTe_2$ films were grown by electron-beam evaporation of Ni (99.9%, Goodfellow Cambridge Ltd.) together with atomic Te flux (99.99%, Sigma-Aldrich) supplied from a Knudsen cell, at a substrate temperature of ~510 K. During growth, a Te flux approximately one order of magnitude higher than that of Ni was maintained to ensure Te-rich conditions. Post-annealing was carried out at ~600 K to induce the formation of self-intercalated phases. The de-intercalation process was achieved by annealing at ~510 K under Te-rich conditions.

LEED, AES and XPS. After growth, the $NiTe_2$ sample was *in-situ* checked by low-energy electron diffraction and Auger electron spectroscopy. LEED was employed with a 4-grid detector (*Omicron Spectra LEED*) in a UHV chamber (1×10^{-9} mbar) at room temperature, which was equipped in the same chamber of MBE. The AES spectra were obtained using an electron-beam energy of 3 kV. The samples were then stored in a home-made UHV suitcase and transferred to the XPS chamber for elemental composition analysis. The high-resolution XPS measurements were carried out at the photoelectron spectroscopy end-station of the Beijing Synchrotron Radiation Facility 4B9B beamline, using a hemispherical energy analyzer. The photon energy was calibrated by referencing the Au 4*f* core level of a clean polycrystalline gold foil electrically connected to the sample.

STM/STS. STM/STS experiments were conducted in an ultrahigh vacuum (UHV) system with a base pressure of 1×10^{-10} mbar. The sample temperature could be stably maintained at base temperatures of 0.4 K and 4.2 K, respectively. In FER spectroscopy, the sample was positively biased. Resonant tunnelling takes place when the Fermi level of the tip aligns with the Stark-shifted image-potential states, resulting in distinct peaks in the dI/dV spectra[51]. All scanning parameters (including setpoint voltage and current) for STM topographic imaging are detailed in the figure captions. Unless otherwise specified, differential conductance (dI/dV) spectra were acquired using a standard lock-in amplifier with a modulation frequency of 973.1 Hz. Tungsten tips were fabricated via electrochemical etching and calibrated on a clean Au(111) surface, which was prepared by repeated cycles of argon ion sputtering followed by annealing at 770 K.

DFT calculations

The DFT calculations in this study were performed with the Vienna Ab-initio Simulation Package (VASP)[52] where the core-valence-electron interactions were described via the projected-augmented-wave (PAW) method[53]. The wave functions were expanded in a plane-wave basis using a 400 eV energy cutoff. Exchange and correlation effects were described using the Perdew-Burke-Ernzerh[54] generalized gradient approximation including van-der-Waals corrections via Grimme's DFT-D3 method[55]. The supercell was simulated using a model of $\sqrt{3}\times\sqrt{3}$ $NiTe_2$ with a vacuum layer of 20 Å. All atoms are fully relaxed until the net force is smaller than 0.02 eV/Å. The k-points sampling is $5 \times 5 \times 1$ with the Gamma scheme.

Data availability

Data measured or analyzed during this study are available from the corresponding author on reasonable request.

Acknowledgements

This work is supported by grants from the National Key Research and Development Projects of China (2022YFA1204100), the National Natural Science Foundation of China (62488201, 52572188, 92580202), the CAS Project for Young Scientists in Basic Research (YSBR-053 and YSBR-003).

Author Contributions: H.J.G, H.C. and H.G. designed the experiments. H.G., Q.F., and R.Z. fabricated the samples and performed LEED and AES measurements. C.L. did the XPS measurements. H.C., Z.H., X.L., L.H., and X.H. performed STM experiments. L.T. did DFT calculations. All of the authors participated in analyzing the data, plotting figures, and writing the manuscript.

Competing Interests: The authors declare that they have no competing interests.

References

[1] Manzeli S, Ovchinnikov D, Pasquier D, Yazyev O V, and Kis A 2017 *Nat. Rev. Mater.* **2** 17033

[2] Lin X, Lu J C, Shao Y, Zhang Y Y, Wu X, Pan J B, Gao L, Zhu S Y, Qian K, Zhang Y F, Bao D L, Li L F, Wang Y Q, Liu Z L, Sun J T, Lei T, Liu C, Wang J O, Ibrahim K, Leonard D N, Zhou W, Guo H M, Wang Y L, Du S X, Pantelides S T, and Gao H-J 2017 *Nat. Mater.* **16** 717

[3] Pan Y, Zhang H G, Shi D X, Sun J T, Du S X, Liu F, and Gao H-J 2009 Adv. *Mater.* **21** 2777

[4] Li G, Zhang Y, Guo H, Huang L, Lu H, Lin X, Wang Y-L, Du S, and Gao H-J 2018 *Chem. Soc. Rev.* **47** 6073

[5] Wang Y, Li L, Yao W, Song S, Sun J T, Pan J, Ren X, Li C, Okunishi E, Wang Y, Wang E, Shao Y, Zhang Y, Yang H, Schwier E, Iwasawa H, Shimada K, Taniguchi M, Cheng Z, Zhou S, Du S, Pennycook S, Pantelides S T, and Gao H-J 2015 *Nano Lett.* **15** 4013

[6] Zeng F, Wang W-B and Tang B-Y 2015 *Chin. Phys. B* **24** 097103

[7] Bian C, Zhao Y, Guzman R, Liu H, Hu H, Qi Q, Zhu K, Wang H, Wu K, Guo H, He W, Wang Z, Peng P, Xu Z, Zhou W, Ding F, Yang H, and Gao H-J 2026 *Nat. Mater.* https://doi.org/10.1038/s41563-026-02495-9

[8] Zhao X, Song P, Wang C, Riis-Jensen A C, Fu W, Deng Y, Wan D, Kang L, Ning S, Dan J, Venkatesan T, Liu Z, Zhou W, Thygesen K S, Luo X, Pennycook S J and Loh K P 2020 *Nature* **581** 171

[9] Guo H, Zhang R, Li H, Wang X, Lu H, Qian K, Li G, Huang L, Lin X, Zhang Y, Ding H, Du S X, Pantelides S T, Gao H-J 2020 *Nano Lett.* **20** 2674

[10] Lasek K, Coelho P M, Zberecki K, Xin Y, Kolekar S K, Li J and Batzill M 2020 *ACS Nano* **14** 8473

[11] Yang R, Mei L, Lin Z, Fan Y, Lim J, Guo J, Liu Y, Shin H S, Voiry D, Lu Q, Li J and Zeng Z 2024 *Nat. Rev. Chem.* **8** 410

[12] Chen H, Bao D L, Wang D F, Que Y D, Xiao W D, Qian G J, Guo H, Sun J T, Zhang Y Y, Du S X, Pantelides S T, and Gao H-J 2018 *Adv. Mater.* **30** 1801838

[13] Rajapakse M, Karki B, Abu U O, Pishgar S, Musa M R K, Riyadh S M S, Yu M, Sumanasekera G and Jasinski J B 2021 *npj 2D Mater. Appl.* **5** 30

[14] Guo H, Wang X, Huang L, Jin X, Yang Z, Zhou Z, Hu H, Zhang Y, Lu H, Zhang Q, Shen C, Lin X, Gu L, Dai Q, Bao L, Du S, Hofer W, Pantelides S T, Gao H-J 2020 *Nano Lett.* **20** 8584

[15] Niu J, Zhang W, Li Z, Yang S, Yan D, Chen S, Zhang Z, Zhang Y, Ren X, Gao P, Shi Y, Yu D and Wu X 2020 *Chin. Phys. B* **29** 097104

[16] Guzman R, Liu H, Bian C, Bao L, Shen C-M, Gao H-J and Zhou W 2024 *Adv. Funct. Mater.* **34** 2401304

[17] Li J, Zhao S, Zhuang L and Hou Y 2025 *Chin. Phys. B* **34** 036301

[18] Liu H, Xue Y, Shi J-A, Guzman R A, Zhang P, Zhou Z, He Y, Bian C, Wu L, Ma R, Chen J, Yan J, Yang H, Shen C-M, Zhou W, Bao L and Gao H-J 2019 *Nano Lett.* **19** 8572

[19] Xie Y, Lv S, Qi Q, Hu G, Zhu K, Zhao Z, Xian G, Han Y, Wang R, Bai C, Bao L, Lin X, Guo H, Yang H, and Gao H-J 2025 *Chin. Phys. B* **34** 087303

[20] Saha R, Meyerheim H L, Göbel B, Hazra B K, Deniz H, Mohseni K, Antonov V, Ernst A, Knyazev D, Bedoya-Pinto A, Mertig I and Parkin S S P 2022 *Nat. Commun.* **13** 3965

[21] Fujisawa Y, Pardo-Almanza M, Garland J, Yamagami K, Zhu X, Chen X, Araki K, Takeda T, Kobayashi M, Takeda Y, Hsu C H, Chuang F C, Laskowski R, Khoo K H, Soumyanarayanan A and Okada Y 2020 *Phys. Rev. Mater.* **4** 114001

[22] Miao G, Gu M, Sun H, Chen P, Li J, Xue S, Su N, Su Z, Zhong W, Zhang Z, Zhu X, Zhang J, Yao Y, Jiang W, Meng M, Wang W, and Guo J 2025 *Adv. Electron. Mater.* **11** 2400720

[23] Liu Y, Liu Y, Dan J, Liu W, Wang L, Hu K, Wang W, Zhang L, Ge B, Du H and Song D 2025 *Adv. Funct. Mater.* **35** 2414699

[24] Wang H, Zhang J, Shen C, Yang C, Küster K, Deuschle J, Starke U, Zhang H, Isobe M, Huang D, van Aken P A and Takagi H 2024 *Nat. Commun.* **15** 2541

[25] Zhang H, Rousuli A, Zhang K, Luo L, Guo C, Cong X, Lin Z, Bao C, Zhang H, Xu S, Feng R, Shen S, Zhao K, Yao W, Wu Y, Ji S, Chen X, Tan P, Xue Q-K, Xu Y, Duan W, Yu P and Zhou S 2022 *Nat. Phys.* **18** 1425

[26] Liu Q, Bai J, Dong Q, Zhang L, Cheng J, Liu P, Li C, Huang Y, Sun Y, Ren Z, and Chen G 2025 *Chin. Phys. B* **34** 017502

[27] Shi M, Kang B, Wu T, and Chen X H 2022 *Chin. Phys. B* **31** 107403

[28] Xu C, Li B, Jiao W-H, Zhou W, Qian B, Sankar R, Zhigadlo N, Qi Y, Qian D, Chou F and Xu X 2018 *Chem. Mater.* **30** 4823

[29] Bhatt N, Ali A, Sharma D, Bansal S, Mandal M, Singh R P and Singh R S 2025 *Phys. Rev. B* **111** 245157

[30] Ferreira P P, Manesco A L R, Dorini T T, Correa L E, Weber G, Machado A J S and Eleno L T F 2021 *Phys. Rev. B* **103** 125134

[31] Zheng F, Li X-B, Tan P, Lin Y, Xiong L, Chen X and Feng J 2020 *Phys. Rev. B* **101** 100505

[32] He C, Zhao J Z, Du M, Zhang L, Zhang J, Yang K, Yuan N, Seliverstov A, Janssens E, Ge J, and Li Z 2025 *Phys. Rev. Lett.* **135** 126607

[33] Zhang J and Huang G 2020 *J. Phys.: Condens. Matter* **32** 205702

[34] Ghosh B, Mondal D, Kuo C-N, Lue C S, Nayak J, Fujii J, Vobornik I, Politano A and Agarwal A 2019 *Phys. Rev. B* **100** 195134

[35] Huang Z, Xian G, Xiao X, Han X, Qian G, Shen C, Yang H, Chen H, Liu B, Wang Z, and Gao H-J 2023 *Nano Lett.* **23** 3274

[36] Hlevyack J A, Feng L-Y, Lin M-K, Villaos R A B, Liu R-Y, Chen P, Li Y, Mo S-K, Chuang F-C and Chiang T-C 2021 *npj 2D Mater. Appl.* **5** 40

[37] Guo H, Huang Z, Gao Y, Chen H, Zhang H, Fang Q, Ye Y, Han X, Cao Z, Wang J, Zhou R, Li Z, Shen C, Yang H, Chen H, Yao W, Wang Z and Gao H-J 2025 *Nat. Commun.* **16** 11327

[38] Anantharaj S, Karthick K and Kundu S 2018 *Inorg. Chem.* **57** 3082

[39] Chia X, Sofer Z, Luxa J and Pumera M 2017 *Chem. Eur. J.* **23** 11719

[40] Shi J, Huan Y, Xiao M, Hong M, Zhao X, Gao Y, Cui F, Yang P, Pennycook S J, Zhao J and Zhang Y 2020 *ACS Nano* **14** 9011

[41] Fazeli Y, Nourbakhsh Z, Yalameha S and Vashaee D 2025 *Nanomaterials* **15** 148

[42] Guo Y, Kang L, Zeng Q, Xu M, Li L, Wu Y, Yang J, Zhang Y, Qi X, Zhao W, Zhang Z and Liu Z 2021 *Nanotechnology* **32** 235204

[43] Zhang L, Chen Z, Zhang K, Wang L, Xu H, Han L, Guo W, Yang Y, Kuo C-N, Lue C S, Mondal D, Fuji J, Vobornik I, Ghosh B, Agarwal A, Xing H, Chen X, Politano A and Lu W 2021 *Nat. Commun.* **12** 1584

[44] Pan S, Hong M, Zhu L, Quan W, Zhang Z, Huan Y, Yang P, Cui F, Zhou F, Hu J, Zheng F and Zhang Y 2022 *ACS Nano* **16** 11444

[45] Binnig G, Frank K H, Fuchs H, Garcia N, Reihl B, Rohrer H, Salvan F and Williams A R 1985 *Phys. Rev. Lett.* **55** 991

[46] Becker R S, Golovchenko J A and Swartzentruber B S 1985 *Phys. Rev. Lett.* **55** 987

[47] Gundlach K H 1966 *Solid-State Electron.* **9** 949

[48] Fowler R H and Nordheim L 1928 *Proc. R. Soc. Lond. A* **119** 173

[49] Schulz F, Drost R, Hämäläinen S K, Demonchaux T, Seitsonen A P and Liljeroth P 2014 *Phys. Rev. B* **89** 235429

[50] Kolesnychenko O, Kolesnichenko A, Shklyarevskii O I and van Kempen H 2000 *Physica B* **291** 246

[51] Borca B and Zandvliet H J W 2024 *Appl. Mater. Today* **39** 102304

[52] Kresse G and Furthmüller J 1996 *Phys. Rev. B* **54** 11169

[53] Kresse G and Joubert D 1999 *Phys. Rev. B* **59** 1758

[54] Perdew J P, Burke K and Ernzerhof M 1996 *Phys. Rev. Lett.* **77** 3865

[55] Grimme S, Ehrlich S and Goerigk L 2011 *J. Comput. Chem.* **32** 1456